



The Ly α Sky as Observed by New Horizons at 57 au

G. Randall Gladstone^{1,2}, J. Michael Shull^{3,4}, Wayne R. Pryor⁵, Jonathan Slavin⁶, Joshua A. Kammer¹, Tracy M. Becker¹, Tod R. Lauer⁷, Marc Postman⁸, John R. Spencer⁹, Joel Wm. Parker⁹, Kurt D. Retherford^{1,2}, Michael A. Velez^{2,1}, Maarten H. Versteeg¹, Michael W. Davis¹, Cynthia S. Froning¹, Camden D. Ertley¹, Nathaniel Cunningham¹⁰, Jayant Murthy¹¹, Richard C. Henry¹², Seth Redfield¹³, Carey M. Lisse¹⁴, Kelsi N. Singer⁹,

Anne J. Verbiscer¹⁵, Pontus C. Brandt¹⁴, and S. Alan Stern⁹

¹ Southwest Research Institute, 6220 Culebra Road, San Antonio, TX 78238, USA; rgladstone@swri.edu

² University of Texas at San Antonio, One UTSA Circle, San Antonio, TX 78249, USA

³ Department of Physics & Astronomy, University of North Carolina, Chapel Hill, NC 27599, USA

⁴ Department of Astrophysical & Planetary Sciences, University of Colorado, Boulder, CO 80309, USA

⁵ Central Arizona College, 8470 North Overfield Road, Coolidge, AZ 85128, USA

⁶ Harvard-Smithsonian Center for Astrophysics, 60 Garden Street, Cambridge, MA 02138, USA

⁷ NSF's National Optical Infrared Astronomy Research Laboratory, P.O. Box 26732, Tucson, AZ 85726, USA

⁸ Space Telescope Science Institute, 3700 San Martin Drive, Baltimore, MD 21218, USA

⁹ Southwest Research Institute, 1301 Walnut Street, Boulder, CO 80302, USA

¹⁰ Physics Department, Nebraska Wesleyan University, Lincoln, NE 68504, USA

¹¹ Indian Institute of Astrophysics, Bengaluru, India

¹² Henry A. Rowland Department of Physics & Astronomy, The Johns Hopkins University, Baltimore, MD 21218, USA

¹³ Astronomy Department, Wesleyan University, Middletown, CT 06459, USA

¹⁴ The Johns Hopkins University Applied Physics Laboratory, 11100 Johns Hopkins Road, Laurel, MD 20723, USA

¹⁵ University of Virginia, Charlottesville, VA 22904, USA

Received 2024 December 19; revised 2025 March 10; accepted 2025 March 11; published 2025 April 25

Abstract

During 2023 September the Alice ultraviolet spectrograph on the New Horizons (NH) spacecraft was used to map diffuse Ly α emission over most of the sky, at a range of ~ 56.9 au from the Sun. At that distance, models predict that the interplanetary medium Ly α emissions result from comparable amounts of resonant backscattering of the solar Ly α line by interstellar hydrogen atoms (H I) passing through the solar system, in addition to an approximately isotropic background of $\sim 50 \pm 20$ R from the local interstellar medium (LISM). The NH observations show no strong correlations with nearby cloud structures of the LISM or with expected structures of the heliosphere, such as a hydrogen wall associated with the heliopause. To explain the relatively bright and uniform Ly α of the LISM, we propose that hot, young stars within the Local Hot Bubble shine on its interior walls, photoionizing H I atoms there. Recombination of these ions can account for the observed ~ 50 R Ly α background, after amplification of the diffuse Ly α by resonant scattering, although sophisticated (i.e., 3D) radiative transfer models should be used to confirm this conjecture. Future observations of the diffuse Ly α , with instruments capable of resolving the line profile, could provide a new window on H I populations in the LISM and heliosphere. The NH Alice all-sky Ly α observations presented here may be repeated at some point in the future, if resources allow, and the two maps could be combined to provide a significant increase in angular resolution.

Unified Astronomy Thesaurus concepts: [Interstellar medium \(847\)](#); [Interstellar scattering \(854\)](#); [Interstellar line emission \(844\)](#)

Materials only available in the [online version of record](#): data behind figure

1. Introduction

Neutral hydrogen atoms (H I) are ubiquitous in the Universe, with a primary allowed electronic transition from $nl = 2p$ to $nl = 1s$ emitting photons at a wavelength of 121.567 nm (i.e., Ly α) which are seen everywhere. In fact, a sizable fraction of the photon energy in our Galaxy (M. Dijkstra 2019) is thought to be carried by Ly α photons. In the local interstellar medium (LISM) these Ly α photons are a million times more likely to undergo resonance scattering than they are to be absorbed by dust, so that very diffuse emissions of Ly α are to be expected. The local Galactic and solar system backgrounds of Ly α emission have been of scientific interest since the space age began (e.g., G. Münch 1962; T. F. Adams 1971; H. J. Fahr 1974). For many years it has been

understood that the Sun resides near a set of low-density clouds of neutral hydrogen atoms (the “Local Fluff” within 10 pc), which are located inside a much larger, low-density cavity the “Local Hot Bubble” (LHB; R. E. Lallement et al. 1986; D. P. Cox & R. J. Reynolds 1987; B. Y. Welsh et al. 1991). A recent survey of molecular clouds and star-forming regions (C. Zucker et al. 2022) suggested that many of these regions lie along the boundary of the LHB. In the inner region of the solar system, any Galactic background at Ly α is dominated by resonantly back-scattered solar Ly α emissions, both in planetary coronas, at brightnesses up to tens of kilorayleighs, where $1 \text{ R} = 1 \text{ rayleigh} = 10^6 \text{ photons cm}^{-2} \text{ s}^{-1} (4\pi \text{ sr})^{-1}$, and in the interplanetary medium (IPM), at brightnesses of 0.5–1 kR near the Earth’s orbit (e.g., J.-L. Bertaux & J. E. Blamont 1971; R. R. Meier 1977, 1991; N. Østgaard et al. 2003). Both are much brighter than the Galactic background of 30–70 R (e.g., G. R. Gladstone et al. 2021).

In this paper, we present the first all-sky maps of diffuse LISM Ly α emissions, produced using the Alice ultraviolet

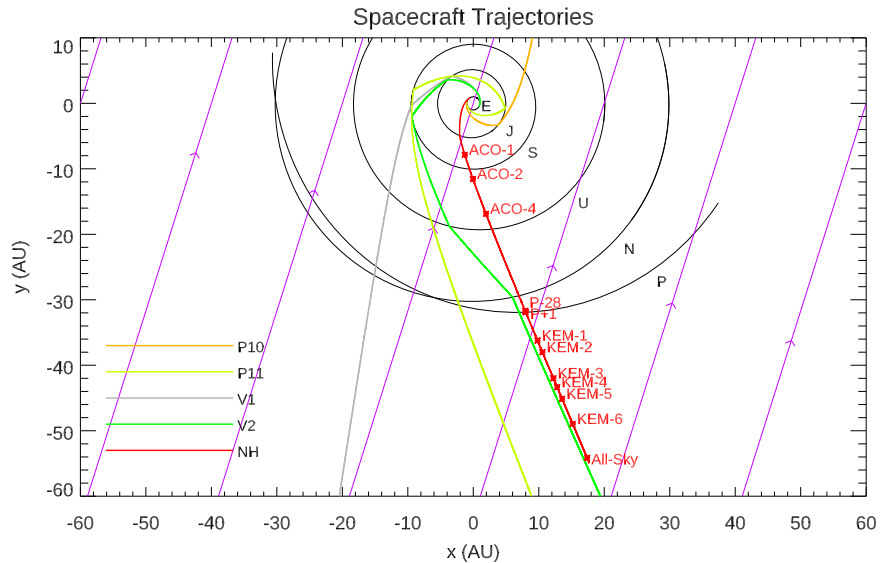


Figure 1. The trajectories of the five spacecraft currently leaving the solar system: Pioneer 10 and 11 (orange and light green, respectively), Voyager 1 and 2 (gray and green, respectively), and New Horizons (NH, red) are shown projected onto the plane of the ecliptic, along with several planet orbits (black) and the direction of the flow of interstellar hydrogen atoms (purple arrows). The locations where great-circle scans of interplanetary medium (IPM) Ly α were made with the NH Alice UV spectrograph are indicated (red), including the all-sky Ly α map described here, which was executed during 2023 September 2–11 at a distance from the Sun of 56.9 au.

(UV) spectrograph on the New Horizons (NH) spacecraft at a range from the Sun of ~ 57 au. The resonantly backscattered solar Ly α brightness falls off nearly inversely with distance from the Sun, and at the current distance of NH it is comparable to the brightness due to the Galactic Ly α background. It is found that the component of the Ly α emission due to backscattered solar Ly α emission by interstellar H I passing through the solar system can be effectively subtracted out using models of that component, leaving a residual brightness map of the Galactic Ly α background that provides a new way to study the structure of the LISM. The residual Ly α emissions are fairly uniform and are not well correlated with known LISM structures, such as the boundaries of local clouds, or with bow shocks which might be expected around fast-moving stars (J. M. Shull & S. R. Kulkarni 2023). The observed 50 ± 20 R of residual Ly α emissions likely results from H atom recombination in the walls of the LHB, following photoionization of those atoms by nearby early-type stars within the LHB and its walls. While the initial source of these emissions would only result in a brightness of ~ 1 R if the Ly α photons were optically thin, resonant scattering amplifies the brightness within the LHB and its walls enough to make the relatively bright and isotropic emissions observed by NH.

2. New Horizons Alice Data

The distant location of the NH spacecraft from the Sun provides a useful platform for observing the diffuse Ly α background of the heliosphere and LISM. Figure 1 shows the NH, Voyager, and Pioneer spacecraft trajectories projected onto the plane of the ecliptic, with the flow of interstellar H I through the solar system indicated for comparison. While more sparse NH observations have been made and discussed earlier (E. Quémerais et al. 2013; G. R. Gladstone et al. 2013, 2015, 2018, 2021), the current results use a much more extensive, nearly all-sky data set which was obtained during 2023 September 2–11 at a range from the Sun of 56.9 au.

For context, Figures 2, 3, and 4 show some of the important features of the LISM, e.g., some of the elements of Figure 1, the walls of the LHB as recently determined (T. J. O’Neill et al. 2024), and nearby stars that are bright at far-ultraviolet (FUV; $91 < \lambda(\text{nm}) < 200$) and extreme-ultraviolet (EUV; $\lambda(\text{nm}) < 91$) wavelengths (see Table 6). Figure 2 also indicates the orientation of the Local Interstellar Cloud (LIC) and G-Cloud in which the Sun is embedded.

The Alice UV spectrograph on the NH spacecraft uses a 4 cm aperture off-axis telescope to feed a Rowland-circle spectrograph, with a double-delay line (or DDL, a particular anode design; see J. V. Vallerga & J. B. McPhate 2000) curved microchannel plate (MCP) detector at the focal plane and electronics and mechanisms in a single unit (S. A. Stern et al. 2008). The entrance slit has a $2^\circ \times 2^\circ$ “box” and a $0.1 \times 4^\circ$ “slot.” The box portion was required by the Alice design in order to assure that the radio and solar occultations at Pluto (which overlapped in time) could be observed together. The Alice spectral bandpass is 52–187 nm with a filled-slit spectral resolution of 0.9 nm in the 0.1 -wide slot. The $2^\circ \times 2^\circ$ is wide enough for off-axis diffuse Ly α emissions to land on KBr and CsI photocathodes which coat the MCP on either side of a bare region of the detector where on-axis Ly α photons fall, giving the spectrograph a high sensitivity to diffuse Ly α emissions (G. R. Gladstone et al. 2015). This sensitivity was initially estimated at $5.5 \text{ counts s}^{-1} \text{ R}^{-1}$ (G. R. Gladstone et al. 2015), and then lowered to $4.92 \pm 0.09 \text{ counts s}^{-1} \text{ R}^{-1}$ (about 11% less than our initial estimate) based on a more careful study (G. R. Gladstone et al. 2021). However, this previous study was not careful enough, as it was discovered in this work that the wrong background count rate was used in the earlier studies. The Alice instrument produces a digital count rate for science observations (using analog counts from the MCP detector which have been further processed by the detector electronics) for science observations, and an analog count rate for housekeeping (using unfiltered analog counts from the MCP detector). It is this analog count rate that is used in the great-circle Ly α observations, in order to save on downlinked

LISM Structure in the Galactic X-Y Plane

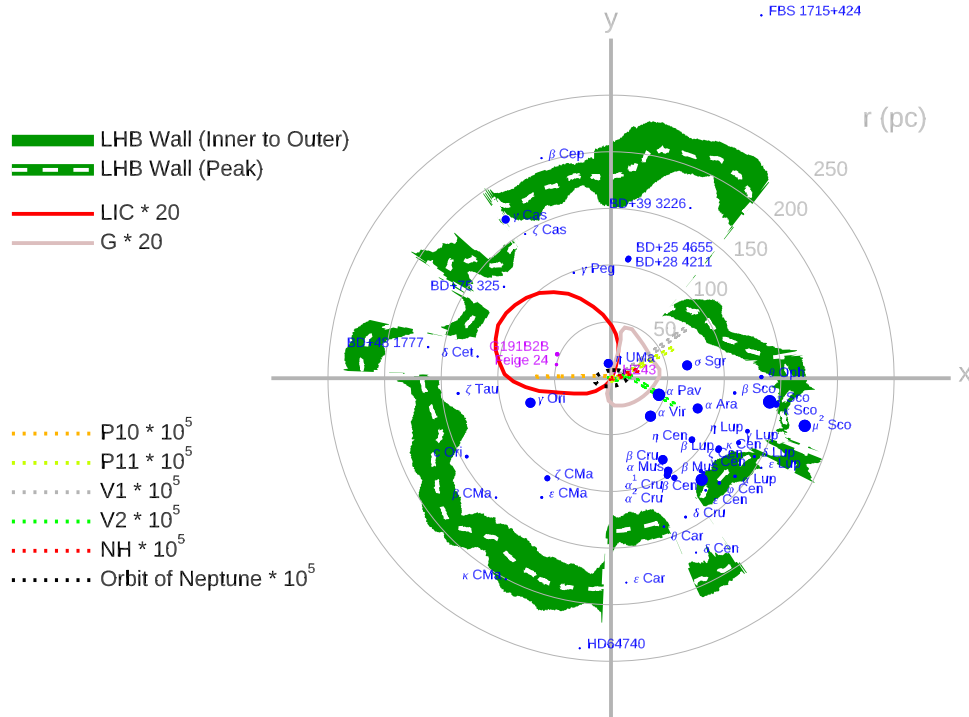


Figure 2. The structure of the local interstellar medium (LISM) is shown in the x - y plane of the Galaxy (where $+x$ is directed toward $(l, b) = (0^\circ, 0^\circ)$ and $+y$ is directed toward $(90^\circ, 0^\circ)$). The green regions show a cross section of the Local Hot Bubble (LHB) wall as provided by T. J. O’Neill et al. (2024), with the inner, peak, and outer surfaces indicated. The outlines of the LIC and G-Cloud (as found by S. Redfield & J. L. Linsky 2008) are shown in red and light brown, respectively, magnified by $20\times$. To indicate the orientation of the solar system and for comparison with Figure 1, the trajectories of the five escaping spacecraft and the orbit of Neptune are projected onto the x - y plane, magnified by $100,000\times$. The locations of 54 UV-bright stars are projected onto the x - y plane, with blue for O and B stars inside the outer wall of the LHB and purple for three nearby EUV-bright white dwarfs (G191B2B, Feige 24, and HZ43).

data volume, a precious resource at the large distance from Earth (and corresponding low data transmission rate) of NH. Since the diffuse Ly α emissions dominate the count rate when no bright stars are in the Alice field of view, we operate the spectrograph as a photometer, and downlink only the total analog count rate observed, with no spectral information. In previous great-circle observations, the data were sent to the ground as housekeeping data, but for the much larger all-sky map discussed here, new flight software was developed to use science frames to hold the analog count-rate data, providing a large savings in data volume. This new software also allows sampling at a higher rate than the maximum 1 Hz rate at which housekeeping data can be taken. For the all-sky map, the sampling rate was set at 10 Hz. Each sample uses 8 bits, so the maximum count rate is $2550 \text{ counts s}^{-1}$. Adjusting for the analog instrument dead time of $4 \mu\text{s}$, the true maximum count rate for the Alice all-sky map is $2576 \text{ counts s}^{-1}$.

Using the proper background, the current estimate of the Alice sensitivity is $3.67 \pm 0.02 \text{ counts s}^{-1} \text{ R}^{-1}$, $\sim 25\%$ less than used in G. R. Gladstone et al. (2021), and the derivation of this value is described in Appendix A. This sensitivity is still $\sim 350\times$ larger than the corresponding sensitivity of the Voyager ultraviolet system (UVS) spectrometers (due to the large solid angle of the Alice box and the high yields of the KBr and CsI photocathodes).

The Alice all-sky map was made by expanding on the six-great-circle concept described in previous studies (G. R. Gladstone et al. 2015, 2021). The sky was scanned in five contiguous 30° segments comprising 15 great circles, with each great circle spaced 2° from

the previous one. The scan rate in the direction perpendicular to the Alice slot was set at $0^\circ 05 \text{ s}^{-1}$, so that each of 75 great-circle observations lasted 2 hr and the entire observation took 150 hr. The 30° segment centered on the Sun (and anti-Sun) was not observed (this would have been segment 3), to protect Alice and co-boresighted instruments from the brightness of the Sun itself.

Some details of the all-sky map segments are provided in Table 1, which includes start and end times in NH Mission Elapsed Time (MET) and Coordinated Universal Time (UTC), scan duration, and the R.A. and decl. of the NH spacecraft’s z -axis (the great-circle axis) at the start of the segment.

At the scan speed of $0^\circ 05 \text{ s}^{-1}$ it takes a point source 2 s to pass through the $0^\circ 1$ width of the slot (providing ~ 20 samples) and 40 s to pass through the 2° width of the box (providing ~ 400 samples). In Figure 5, we provide a close-up of just 5 hr out of the 150 hr of count rates, in which many narrow and very narrow spikes are seen in the count rate due to stars passing through the box and slot, respectively.

While it is not easy to correct for these stars, we are able to remove most of them from the data by sampling the M. A. Velez et al. (2024) star catalog in the same way that the sky was sampled by the Alice instrument and flagging times where stars contaminated the Alice signal in a substantial way. These contaminated data are masked and removed, and the remaining uncontaminated count rates are smoothed by an instrument function based on deep spectra of the dark sky (i.e., the NCOB observations in Table 5 of Appendix A). This instrument function is basically a column integration of the right panel of Figure 9 of Appendix A, with the x -axis

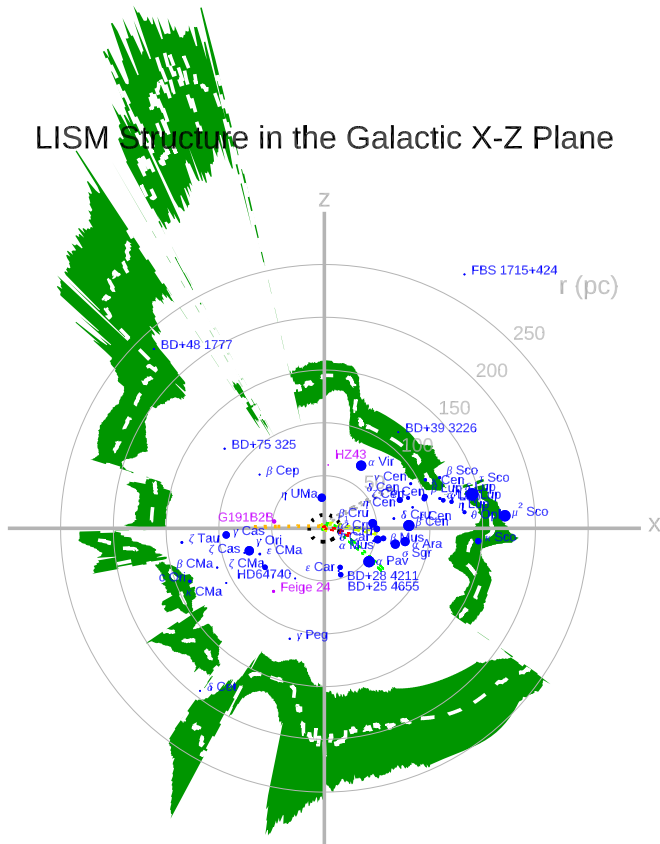


Figure 3. The structure of the local interstellar medium (LISM) is shown in the x - z plane of the Galaxy (where $+x$ is directed toward $(l, b) = (0^\circ, 0^\circ)$ and $+z$ is directed toward $(0^\circ, 90^\circ)$). The rest of the figure is as in Figure 2, except that the outlines of the LIC and G-Cloud are not shown.

converted to time (as mentioned above, the box is ~ 40 s wide as the slit scans a great circle on the sky).

During the all-sky scans the Alice aperture door was preplanned to close if a particularly bright star was passing through the slot or the box portions of the slit. Although these times were only a small portion of the total observations (~ 45 minutes out of ~ 150 hr), they provide our best estimate of the analog dark count rate during the observations, which was determined to be $177 \text{ counts s}^{-1}$ with a Gaussian distribution.

After the count-rate data are preprocessed as described above, maps are made of the sky in both ecliptic and Galactic coordinates, as shown in Figure 6. In these maps the gores (swaths of missing data on the maps) are filled with a model (described below) of the expected signal from resonant backscattering of solar $\text{Ly}\alpha$ plus a 50 R value representative of the Galactic $\text{Ly}\alpha$ background.

3. Maps and Models

We build Figure 6 by first establishing a base map of the modeled sky and then overplotting the Alice observations. The base map can be seen in the gore spaces where we did not acquire Alice data (mostly the 30° gore centered on the Sun, but also the much narrower gores between segments). The base-map model includes only an assumed-constant Galactic $\text{Ly}\alpha$ background plus a model of the resonantly backscattered solar $\text{Ly}\alpha$ brightness, which we refer to as the “Hall” code. As described in G. R. Gladstone et al. (2021), the Hall code is a

hybrid of a “hot model,” i.e., a model of interstellar hydrogen flow through the solar system which accounts for gravity, radiation pressure, photoionization, and H temperature (e.g., G. E. Thomas 1978), but does not account for charge exchange, of the IPM neutral hydrogen properties, run for the specific location of NH at the time of the all-sky observations (e.g., W. R. Pryor et al. 2013), and a full multiple-scattering radiative transfer model adapted from the code described in D. T. Hall (1992) and D. T. Hall et al. (1993). The solar $\text{Ly}\alpha$ line profile used in the model is from P. Lemaire et al. (1978). Resonant scattering of the solar line assumes the complete frequency redistribution (CFR) approximation, with Doppler profiles for absorption and emission. Doppler shifts and widths in the cylindrically symmetric (about the upstream direction) coordinate system are calculated using flow velocities and effective temperatures derived for each model volume element. The radiative transfer equation is solved by successive orders of scattering, which is straightforward for low-optical-depth problems such as scattering of solar $\text{Ly}\alpha$ in the heliosphere.

As in G. R. Gladstone et al. (2021), the parameters for the Hall model of neutral hydrogen density, temperature, and velocity at the outer boundary are taken to be $n_\infty = 0.12 \text{ cm}^{-3}$ (consistent with the recent determination of $n_\infty = 0.127 \pm 0.015 \text{ cm}^{-3}$ by P. Swaczyna et al. 2020), $T_\infty = 12,000 \text{ K}$, and $v_\infty = 20 \text{ km s}^{-1}$ (consistent with the Solar and Heliospheric Observatory, or SOHO, Solar Wind ANisotropy Experiment hydrogen absorption cell measurements of J. Costa et al. 1999). Likewise, the solar $\text{Ly}\alpha$ flux at the sub-NH solar longitude available for scattering from interstellar wind hydrogen, the radiation pressure parameter (μ), and the total expected hydrogen atom lifetime at 1 au were estimated using data from the solar $\text{Ly}\alpha$ database at the University of Colorado Laboratory for Atmospheric and Space Physics (T. Woods et al. 2000). The Hall model does not include the hydrogen wall that is expected in the outer heliosphere by more state-of-the-art codes (e.g., V. B. Baranov et al. 1991; V. B. Baranov & G. Malama 1993; V. V. Izmodenov et al. 2013; E. Quémerais et al. 2010; E. Quémerais et al. 2013; O. A. Katushkina et al. 2016, 2017). The hydrogen wall forms during charge exchange between interstellar H I and interstellar protons that have been decelerated and deflected as they approach the heliopause.

Since the Hall model used to estimate the backscattered solar $\text{Ly}\alpha$ and the assumption of an isotropic Galactic background are each imperfect, we have scaled both in order to provide the best fit to the map data of Figure 6 in the regions of the gore boundaries. We apply a scale factor of $1.6\times$ to the Hall model brightness map, and include an isotropic Galactic component of 50 R (up from the 43 R found in G. R. Gladstone et al. 2021). Although this was not done in a rigorous way, the fit as shown is quite reasonable (e.g., it is hard to see the gore boundaries, except in the anti-Sun hemisphere where the model is a few rayleighs fainter than the observations; the gore locations are clearly shown in Figure 7). Remaining differences between the model and data at the gore boundaries could reasonably be due to the Galactic $\text{Ly}\alpha$ actually being anisotropic and/or assumptions made in the Hall model (e.g., the CFR approximation).

The maps in Figure 6 show no large-scale brightness structure that might be associated with the presence of a hydrogen wall (e.g., E. Quémerais et al. 2010; V. V. Izmodenov et al. 2013) in the direction of the nose of the heliopause (i.e., centered near the location marked “IPM Upstream” in the both the ecliptic

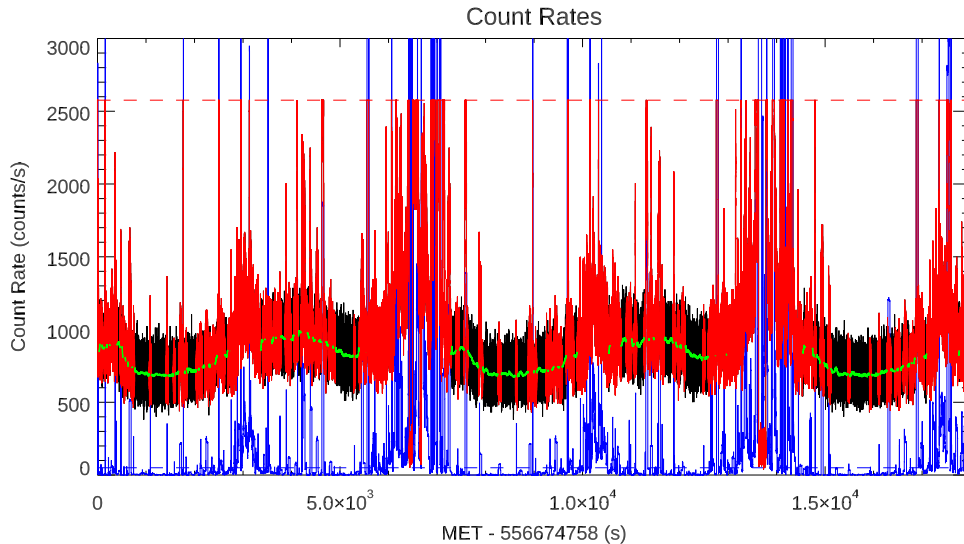


Figure 5. A 5 hr excerpt from the ~ 150 hr of data is used to illustrate how the data were processed prior to making the all-sky map. The raw 10 Hz count-rate samples are shown in black. The blue line shows the expected count rate due to stars passing through the Alice slit, using the Velez et al. (2024) star catalog. We take any data at times where this expected stellar count rate is >50 counts s^{-1} (shown as a horizontal dashed blue line) as contaminated (here marked red) and remove them. We then smooth the remaining uncontaminated data using an instrument function which is approximately a smoothed boxcar of ~ 40 s (i.e., ~ 400 samples) length. The final count rate is shown in green, and is linearly interpolated across gaps due to star contamination. The horizontal red dashed line indicates the maximum Alice count rate during the all-sky map of 2576 counts s^{-1} .

of their astrospheres (although such structures could be present at the 2–8 R level predicted by J. M. Shull & S. R. Kulkarni 2023). Instead, the $Ly\alpha$ map is dominated by large, low-order brightness variations away from the Galactic disk, where contamination by stars is very difficult to eliminate, and also away from the Sun. These regions are more extensive in the southern Galactic hemisphere than in the northern Galactic hemisphere. Smaller-scale features include the “haloes” surrounding very bright and nearby stars (e.g., α Pav and α Eri at southern Galactic latitudes, α Vir and ι Her at northern Galactic latitudes).

After scaling the backscattered solar $Ly\alpha$ to give a reasonable fit the Alice $Ly\alpha$ brightness map, we subtract the model solar contribution (i.e., the Hall model, which is the same as the base map minus the assumed-constant 50 R background) to see the underlying structure of the Galactic $Ly\alpha$ emission. These residual $Ly\alpha$ maps are plotted in Figure 7. In this figure the dynamic range of the color bar has been reduced by a factor of $10\times$ (i.e., from 500 R down to 50 R), in order to bring out details, but it is important to keep in mind that 25–75 R is a very small range in brightness and brings out artifacts (especially at low Galactic latitudes, where the stellar contamination is very large). Nevertheless, there appear to be few, if any, good correlations between the residual $Ly\alpha$ maps and any of the structures we might expect to show up, i.e., cloud boundaries, shocks associated with fast stars, or a hydrogen wall structure. The main feature of the residual all-sky $Ly\alpha$ map is its general smoothness, along with a rather high level for the average emission brightness of $\sim 50 \pm 20$ R.

Since the most useful data are at high Galactic latitudes, we also present residual $Ly\alpha$ maps for the regions of the north and south Galactic poles in Figure 8. Apart from some haloes surrounding a few bright stars, the polar regions are observed to be very uniform, with only a small brightness gradient of ~ 10 R across $>60^\circ$ of latitude. The north polar region is typically ~ 10 R brighter than the south polar region, i.e., ~ 50 R compared to ~ 40 R.

We now consider what the sources of the diffuse $Ly\alpha$ are in the LISM, beginning with an overview of how $Ly\alpha$ photons scatter in small and large LISM clouds. The solar system is embedded in (or near) two small clouds (the LIC and the G-Cloud; S. Redfield & J. L. Linsky 2008), and one large cloud (the walls of the LHB). Multiple scattering of $Ly\alpha$ photons inside a sufficiently optically thick cloud that surrounds the solar system would provide a simple way to make the diffuse emissions more isotropic, as observed in the NH maps.

4. $Ly\alpha$ Radiative Transfer in the Local Interstellar Medium

To understand where the Galactic $Ly\alpha$ emissions originate, it is important to understand how $Ly\alpha$ photons scatter in the LISM. The sources of $Ly\alpha$ from recombination of H I atoms following photoionization are only sufficient to produce a few rayleighs of brightness, if the $Ly\alpha$ photons were optically thin. However, the brightness level inside a cloud (or, as for the LHB, an empty shell) of H I atoms can be amplified by resonant scattering, if the cloud or shell is sufficiently optically thick. In this section, we examine the scattering parameters of small clouds, such as the LIC or G-Cloud, and larger structures, such as the walls of the LHB.

For a spherical cloud, with a $Ly\alpha$ optical depth of τ_0 at line center, we can relate the number of photon scatterings N_s and mean free path λ_{mfp} for line scattering opacity to the escape of $Ly\alpha$ into the optically thin damping wings. The Doppler profile is characterized by a thermal velocity parameter,

$$b = (2kT/m_H)^{1/2} = (10.76 \text{ km s}^{-1}) T_{7000}^{1/2}, \quad (1)$$

at $T = (7000 \text{ K})T_{7000}$, and the Doppler width of $Ly\alpha$ in frequency is

$$\Delta\nu_D = b\nu_0/c = b/\lambda_0 \approx (8.85 \times 10^{10} \text{ Hz})T_{7000}^{1/2}. \quad (2)$$

The intrinsic line width (Lorentzian width) is given by

$$\Delta\nu_L = A_{21}/2\pi \approx 9.97 \times 10^7 \text{ Hz}, \quad (3)$$

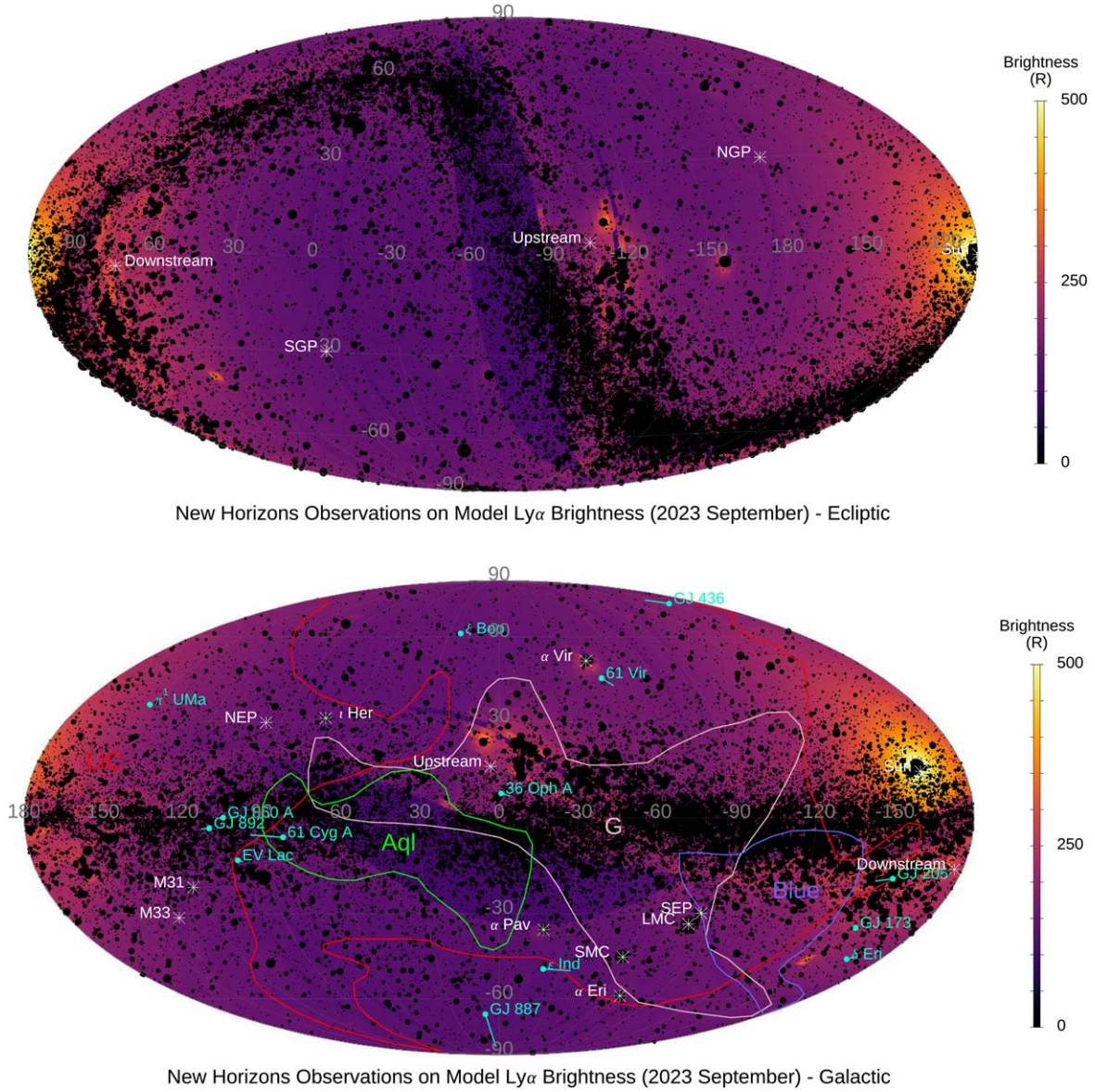


Figure 6. All-sky New Horizons Alice Ly α maps derived from analog count rates (as processed in the manner described in Figure 5) and converted to brightness using the sensitivity value of $3.67 \text{ counts s}^{-1} \text{ R}^{-1}$ ($1 \text{ R} = 10^6 \text{ photons cm}^{-2} \text{ s}^{-1} (4\pi \text{sr})^{-1}$) that is derived in Appendix A. The upper map is in ecliptic coordinates centered on the anti-Sun direction, and the lower map is in Galactic coordinates, centered on $(l, b) = (0^\circ, 0^\circ)$. Both Mollweide projection maps show Alice brightnesses (except for the 30° swath containing the Sun, which shows a hot model estimate of the backscattered solar Ly α plus a 50 R value meant to represent the Galactic Ly α signal). The $\sim 90,000$ stars in the M. A. Velez et al. (2024) catalog are overlaid as black dots, where the size of the dot is proportional to the logarithm of the expected Alice count rate from each star. The map in Galactic coordinates indicates the outlines of four of the important LISM clouds (“LIC,” in red; “Aql,” in green; “Blue,” in blue; and “G,” in tan), as described in S. Redfield & J. L. Linsky (2008). The locations of 14 fast-moving stars from J. M. Shull & S. R. Kulkarni (2023), listed here in Table 2, are indicated by light blue dots, with lines extending to their expected locations in 10^4 yr. Both maps also include directions for the poles of the alternate projection map, the upstream and downstream directions of the flow of interstellar H I through the solar system, and the Sun. The Galactic All-sky New Horizons Alice Ly α map shown in panel (b) of this figure is available as data behind figure in FITS format. These data can also be used to obtain the results shown in Figure 7(b).

(The data used to create this figure are available in the [online article](#).)

for a radiative decay rate of $A_{21} = 6.265 \times 10^8 \text{ s}^{-1}$. From these frequency widths the Voigt damping parameter (see M. Dijkstra 2014) is given by

$$a \equiv \Delta\nu_L/2\Delta\nu_D = (5.63 \times 10^{-4})T_{7000}^{-1/2}. \quad (4)$$

We now switch to using the dimensionless frequency $x = (\nu - \nu_0)/\Delta\nu_D$ away from line center at frequency ν_0 and wavelength $\lambda = 121.567 \text{ nm}$. The line profile (Voigt function)

can be approximated by

$$\phi(x) = \exp(-x^2) \quad (5)$$

in the Doppler core and

$$\phi(x) \approx a/\sqrt{\pi}x^2 \quad (6)$$

in the damping wings. The dividing point between these regimes occurs at a dimensionless frequency $x_{\text{crit}} \approx 3.2$ for $T = 7000 \text{ K}$ and $a/\sqrt{\pi} = 3.18 \times 10^{-4}$. Diffusive scattering of Ly α emission

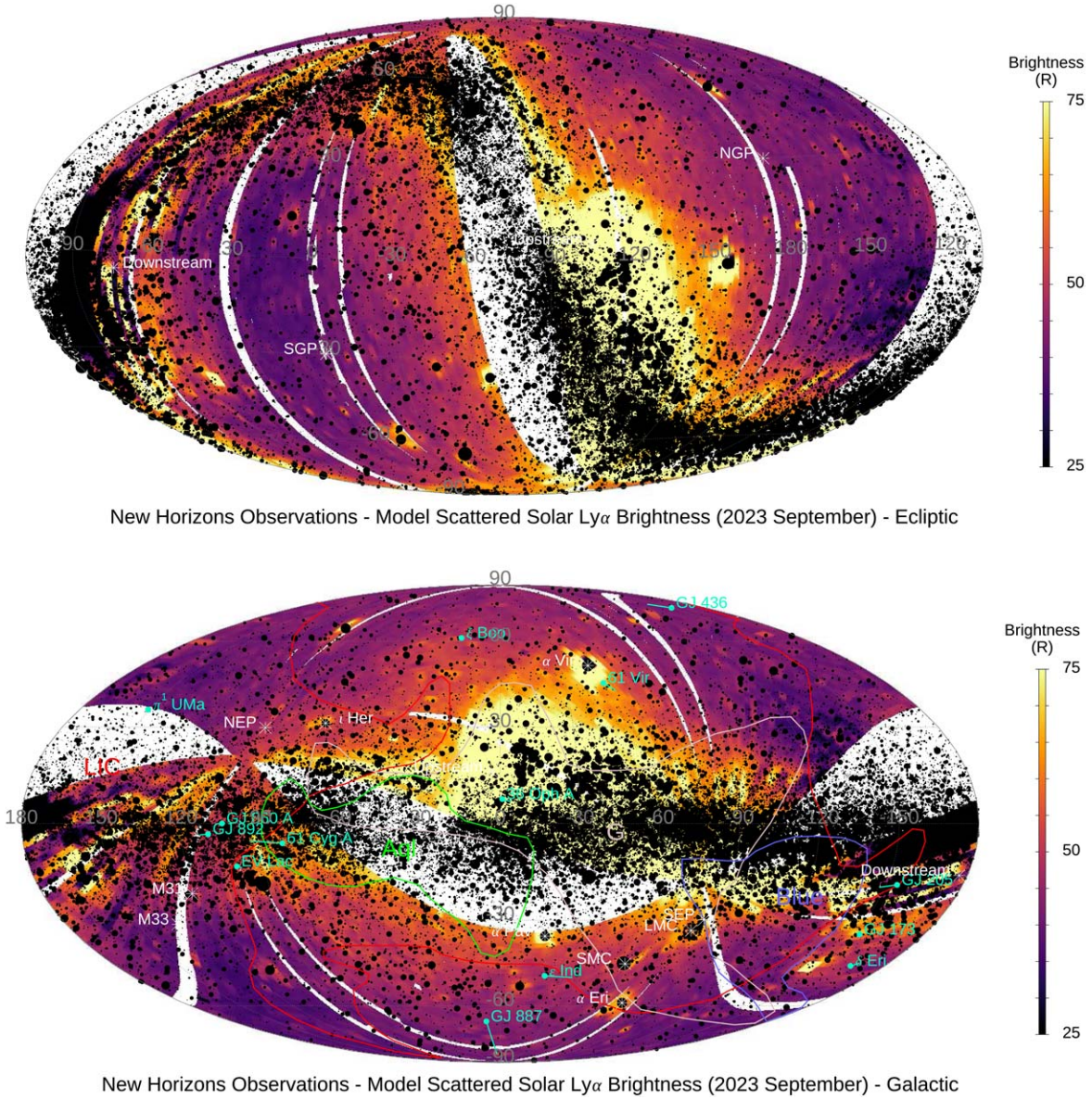


Figure 7. The all-sky NH Ly α maps are constructed in the same way as for Figure 6, but show the residual brightness after subtracting a model prediction of the backscattered solar Ly α . Note that the range in brightness has been reduced to only 25–75 R in these residual maps.

lines in extremely optically thick media occurs at large values of the product

$$a\tau_0 > 10^3. \quad (7)$$

In this process, photons scatter repeatedly within the Doppler core of the line, and undergo a random walk in frequency space into the wings. The mean free path of a wing photon at frequency x is

$$\lambda_{\text{mfp}} \sim 1/\phi(x) \quad (8)$$

in units of line-center optical depth τ_0 . Photons in the line wing scatter $N_s \sim x^2$ times, usually returning to the core. After many scatterings, the photons gradually shift out of the Doppler core into the optically thin damping wings. At that point, the photon mean free path becomes comparable to the cloud size, allowing photons to escape.

As the Ly α photon scatters repeatedly within the Doppler core, standard random-walk arguments show that the photon

moves to a dimensionless frequency in the damping wings, $x_s \approx N_s^{1/2}$, in steps of the mean free path, λ_{mfp} . At this point, a photon will have diffused a “distance” $N_s^{1/2}/\phi(x)$ away from the cloud center (measured in line-center optical depths). When we set this distance to the cloud line-center optical depth,

$$N_s^{1/2}/\phi(x) = \tau_0, \quad (9)$$

and use the approximation

$$\phi(x) \approx a/\sqrt{\pi}x^2 \quad (10)$$

appropriate for the damping wings, we find the scaling relation

$$x_s \approx (a\tau_0/\sqrt{\pi})^{1/3}. \quad (11)$$

M. Dijkstra (2014) notes that one expects a self-reversed line profile for Ly α photons emerging from the center of any extremely opaque object, with two emission peaks in the line

Table 2
Nearby Fast Stars

Name	$V_{\text{ISM}}^{\text{a}}$ (km s^{-1})	R.A. (deg)	Decl. (deg)	l (deg)	b (deg)	$l_{+10 \text{ kyr}}^{\text{b}}$ (deg)	$b_{+10 \text{ kyr}}^{\text{b}}$ (deg)
61 Cyg A	86	316.725	38.503	82.135	-5.983	94.518	-5.265
GJ 887	85	346.467	-34.147	9.227	-66.310	4.614	-82.560
GJ 436	79	175.546	26.707	210.542	74.569	220.986	76.392
GJ 205	70	82.864	-2.323	205.666	-18.818	212.162	-19.573
ϵ Ind	68	330.840	-55.214	338.317	-48.739	324.524	-49.347
61 Vir	51	199.601	-17.689	311.986	44.708	307.687	42.089
GJ 892	49	348.321	57.168	109.899	-3.199	113.089	-3.443
GJ 860 A	47	336.752	57.695	104.575	0.065	103.326	0.124
EV Lac	45	341.707	44.334	100.607	-13.069	98.696	-13.493
π^1 UMa	43	129.799	65.021	150.552	35.704	150.267	35.621
36 Oph A	40	258.837	-25.470	359.214	7.528	355.873	6.682
GJ 173	38	69.425	-10.961	207.533	-34.620	207.810	-35.412
δ Eri	37	55.812	-8.237	196.195	-45.235	193.519	-44.375
ξ Boo A	32	222.847	19.100	23.086	61.356	23.128	61.004

Notes.

^a V_{ISM} is the ISM flow speed in the stellar rest frame (J. M. Shull & S. R. Kulkarni 2023).

^b Expected location of star in 10,000 yr.

wings on either side of line center at frequencies

$$x_p \approx \pm k(a\tau_0/\sqrt{\pi})^{1/3}, \quad (12)$$

in dimensionless $\Delta\nu_D$ units, where $k \approx 1.1$ for a slab and $k \approx 0.92$ for a sphere.

Applying these expressions first to the small local clouds within 10 pc, with typical temperatures $T \approx (7000 \text{ K})T_{7000}$ and neutral H column densities $N_{\text{HI}} = (10^{18} \text{ cm}^{-2})N_{18}$ (S. Redfield & J. L. Linsky 2008; J. L. Linsky & S. Redfield 2021), we find line-center optical depths

$$\tau_0 = \left(\frac{\pi e^2}{m_e c} \right) \frac{N_{\text{HI}} f \lambda}{\sqrt{\pi} b} \approx (70,440) N_{18} T_{7000}^{-1/2}, \quad (13)$$

where b is as given above, the oscillator strength $f = 0.4164$, and $(\pi e^2/m_e c) = 0.02654 \text{ cm}^2 \text{ s}^{-1}$. The critical parameter

$$a\tau_0 \approx 40 \ll 10^3 \quad (14)$$

for these small clouds, indicating that scattering into the damping wings is only partially complete. The characteristic dimensionless scattering frequency would be

$$x_s \approx 2.8 N_{18}^{1/3} T_{7000}^{-1/6}. \quad (15)$$

Thus, it seems that the small local clouds are not optically thick enough to isotropize any Ly α photons incident on or created within them.

Now we consider the higher-density walls of the LHB. If we parameterize the shell with HI column density $N_{\text{HI}} = (10^{20} \text{ cm}^{-2})N_{20}$, the same formalism for Ly α scattering gives line-center optical depths of

$$\tau_0 = (7.0 \times 10^6) N_{20} T_{7000}^{-1/2}. \quad (16)$$

The critical parameter for the LHB walls is

$$a\tau_0 \approx 3940 > 10^3 \quad (17)$$

so that scattering into the damping wings is complete, and the characteristic dimensionless scattering frequency is

$$x_s \approx 13 N_{20}^{1/3} T_{7000}^{-1/6}. \quad (18)$$

The neutral hydrogen at the LHB walls could be cooler than the assumed 7000 K, but the $T^{-1/6}$ dependence of x_s is weak. The Ly α in the LHB walls is expected to be extremely optically thick, approaching 10^7 line scatterings out to a dimensionless frequency $x_s \sim 10$ –20 in the line wings. These lines will effectively be in the FUV continuum near $\lambda \sim 121.6 \text{ nm}$ and subject to dust absorption over length scales of a few hundred parsecs. In the C. Zucker et al. (2022) model, the estimated shell of displaced gas has a mass $M_{\text{sh}} \approx 1.4 \times 10^6 M_{\odot}$ and average radius $R_{\text{sh}} \approx 165 \text{ pc}$. The mean (total hydrogen) column density would be

$$N_{\text{H}} \approx \frac{M_{\text{sh}}}{4\pi R_{\text{sh}}^2 (1.4 m_{\text{H}})} \approx 3.7 \times 10^{20} \text{ cm}^{-2}, \quad (19)$$

distributed over phases of H I, H II, and H₂. They model the mean hydrogen density of the ambient (displaced) gas to be $n_{\text{H}} \approx 2.71_{-1.02}^{+1.57} \text{ cm}^{-3}$. The large shell of hydrogen at the walls of the LHB does seem to be optically thick enough to isotropize Ly α photons created within it.

Besides a large column of neutral H to scatter Ly α photons, an initial source of photons is required. As with early studies (e.g., G. Münch 1962), we expect that most initial Ly α photons result from recombination of regions photoionized by O and B stars. Many such stars are found in the LHB (see Table 6), and there are several nearby clusters of recently formed stars in and near the walls of the LHB. Many of these star clusters appear toward one general direction, at Galactic longitudes of $l \approx 353^\circ$ (Ophiuchus Cloud at $d \approx 140 \text{ pc}$), $l \approx 351^\circ$ (Sco-Cen Association at $d \approx 130 \text{ pc}$), and $l \approx 359^\circ$ (Corona Australis Association at $d \approx 125 \text{ pc}$). Other potentially bright regions include the Taurus Association ($l \approx 174^\circ$, $d \approx 140 \text{ pc}$), Pleiades Cluster ($l \approx 167^\circ$, $d \approx 135 \text{ pc}$), and Hyades Cluster ($l \approx 180^\circ$, $d \approx 46 \text{ pc}$). Much of the photoionization from these hot star clusters in the LHB wall is expected to result in Ly α emission through recombination. Based on the scattering arguments above, any Ly α that gets through the LHB wall and is detected by the Alice spectrograph should be far enough into the line wings that no further resonant scattering within the smaller nearby clouds would be expected.

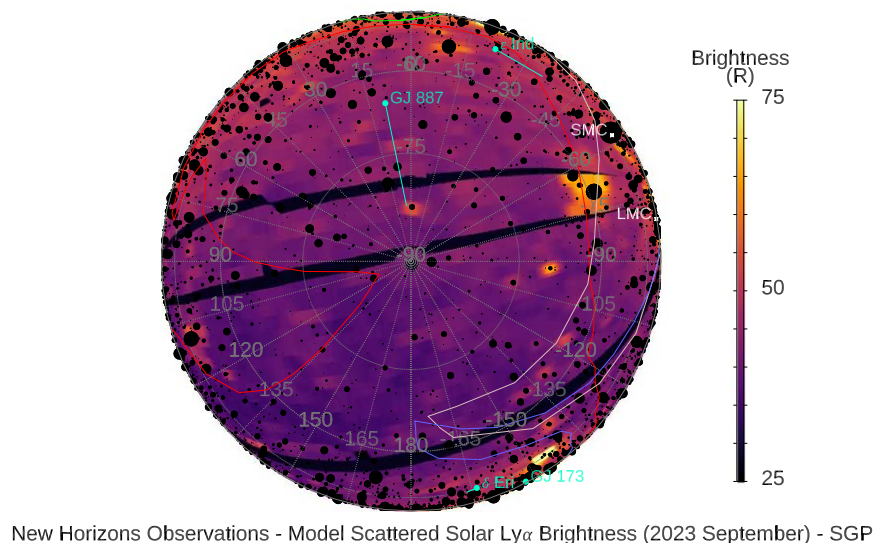
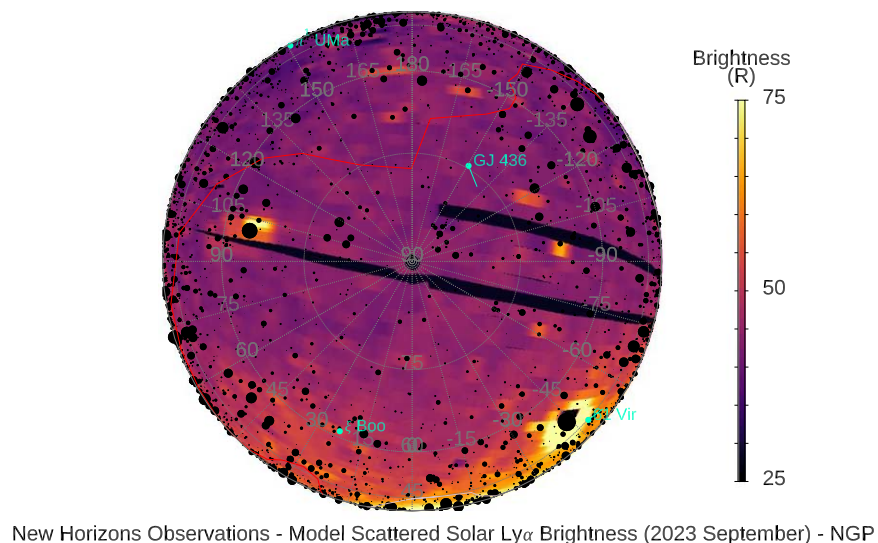


Figure 8. Residual Ly α maps in Galactic coordinates, showing the polar regions (in satellite projection) for the north Galactic pole (NGP, upper) and south Galactic pole (SGP, lower). The typical diffuse brightness is ~ 5 – 10 R larger in the north than in the south.

Table 3
Absent Structures in Residual Ly α Map

Feature	Lack of Expected Structure	Possible Explanation
Hydrogen wall	No significant brightening in the direction of the helio-pause, suggesting no detectable hydrogen wall enhancement.	A hydrogen wall could exist but be too faint and/or diffuse to be detected with the current data set.
LISM clouds	No clear correlation between Ly α emissions and the expected density gradients of the LIC and G-Cloud.	Ly α emissions from the wall of the LHB may be shifted by resonance scattering far enough from line center that they are not scattered by the LISM clouds. However, unresolved small-scale variations in local cloud structure could still affect the Ly α brightness. Also, cloud boundary uncertainties could affect the correlation analysis (see C. Gry & E. B. Jenkins 2014).
Fast-moving stars	Absence of localized Ly α enhancements around high-velocity stars suggests minimal bow-shock excitation.	Bow-shock Ly α emissions could be below the detection threshold or be present but unresolved at the coarse spatial resolution of the Alice map.

5. Discussion

The residual Ly α maps presented earlier (Figures 7 and 8) show mostly smooth variations at higher Galactic latitudes, with no apparent correlations with any LISM structures that we had expected to see. A summary of these absent structures is

provided in Table 3. We believe that the lack of correlations and the general smoothness of the residual Ly α brightness map is best explained by resonant scattering of Ly α photons in the walls of the LHB. The Ly α brightness seen from the location of the solar system near the center of the LHB are those photons

Table 4
Important Assumptions

Key Assumption	Description	Potential Limitations
Calibration and sensitivity of Alice spectrograph	Alice’s sensitivity calibration is assumed to be accurate for Ly α brightness conversion.	Background subtraction uncertainties and potential instrumental degradation over time may affect absolute brightness estimates.
Hall model	This model accounts for backscattered solar Ly α , which is subtracted from the observed Ly α brightness to produce the residual Ly α map.	The Hall model neglects charge-exchange reactions, and so does not include a hydrogen wall. It also includes the simplifying but inaccurate assumptions of CFR in its resonant scattering calculations, and cylindrical symmetry about the upstream/downstream axis.
Uniformity of residual Ly α emission	Residual Ly α brightness (50 ± 20 R) is interpreted as a uniform background from recombination in LHB walls, followed by resonant scattering.	Localized variations in ionizing sources or extragalactic contributions could introduce small-scale structure. A 3D radiative transfer model is needed.
Resonant scattering and optical depth	The LHB walls are assumed to be highly optically thick at line center ($\tau \sim 10^7$), ensuring multiple scattering that can isotropize Ly α .	Small-scale density variations or turbulence in the LHB walls could introduce anisotropies in Ly α emission. A 3D radiative transfer model is needed.

which have escaped from some location on the interior wall of the LHB and were passing through the bubble toward another location on the interior LHB wall. The initial source of the Ly α photons in the LHB walls is recombination of protons and electrons following photoionization of neutral hydrogen atoms in the LHB walls by EUV radiation produced by hot stars in the LHB and within its walls.

Based on the above scattering arguments for distant Ly α emissions, the relatively isotropic nature of the residual Ly α map emissions indicates that they are likely produced in the nearby LISM, specifically in the walls of the LHB. If the final emissions after multiple scattering are isotropic and homogeneous, the radiative transfer equation becomes simpler. Since the radiation does not change along any given line of sight and because scattering losses along that direction are balanced by scattering gains from other directions, we can write (see G. E. Thomas & J. E. Blamont 1976)

$$J \approx k_{\text{abs}} 4\pi I, \quad (20)$$

where J is the initial volume emission rate of Ly α photons in the nearby LHB walls, $4\pi I$ is the Galactic background of 50 R (i.e., 5.0×10^7 photons $\text{cm}^{-2} \text{s}^{-1}$), and k_{abs} is the average coefficient for pure absorption by dust at $\lambda = 121.6$ nm, which is approximately $6.9 \text{ kpc}^{-1} = 2.24 \times 10^{-21} \text{ cm}^{-1}$ (from B. T. Draine 2011, and assuming a dust Ly α albedo of 0.5) for the LHB walls, using the parameters given above from C. Zucker et al. (2022) and updated in T. J. O’Neill et al. (2024). Thus, in order to produce the observed brightness of nearly isotropic Ly α emissions we need an initial Ly α volume emission rate of $J \sim 5 \times 10^7 \times 2.24 \times 10^{-21} \sim 1.1 \times 10^{-13}$ photons $\text{cm}^{-3} \text{s}^{-1}$ or more. While the ionization rate at the LHB walls will vary with location, a typical value might be what is measured in the solar system. Using the M. A. Velez et al. (2024) stellar catalog and the T. J. O’Neill et al. (2024) LHB wall distances, we find 54 stars that contribute most to the local ionization rate of $\Gamma_{\text{HI}} \sim 6 \times 10^{-13} \text{ s}^{-1}$ (see Table 6 of Appendix B for details). For an LHB wall neutral H density of $n_{\text{HI}} \sim 3 \text{ cm}^{-3}$, a typical photoionization rate at the inside wall of the LHB would be $\sim 1.8 \times 10^{-12} \text{ cm}^{-3} \text{ s}^{-1}$. In photochemical equilibrium, the initial Ly α volume emission rate would be ~ 0.68 of the photoionization rate or $J \sim 1.2 \times 10^{-12}$ photons $\text{cm}^{-3} \text{ s}^{-1}$, which should be more than enough to produce the observed residual Ly α brightness.

Photoionization at the LHB walls from the hot gas within the bubble also contributes (see Figure 2 of P. C. Frisch et al. 2011) but is neglected here since stellar photoionization dominates. As noted in the analysis of the EUV spectrum of ϵ CMa by J. M. Shull et al. (2025), for most early-type stars there is a decrement of EUV flux near the Lyman limit at 91.1 nm, which may be inaccurately simulated in the Kurucz model (LTE) fits to the observed FUV flux used in the M. A. Velez et al. (2024) catalog. This would mean that our estimated photoionization rate could be substantially underestimated.

It is important to note that Ly α photons undergoing resonance-line radiative transfer in the walls of the LHB are able to move freely back and forth across the cavity inside the walls without being absorbed or scattered by the hot ionized gas in the LHB (although each crossing will take several hundred years). Thus, inside the LHB at the location of the solar system, the local Ly α is amplified by multiple scattering so that what would provide an optically thin brightness of ~ 1 R is increased to an optically thick value of ~ 50 R within the LHB. We have run simple “slab” plane-parallel models of the LHB walls, using the angle-averaged partial frequency redistribution resonance scattering code of G. R. Gladstone (1982) with a midplane initial volume emission rate and LHB wall model consistent with the above estimates, and confirm that an amplification factor of ~ 50 is relatively easy to achieve (while similar models for the LIC and G-Cloud are unable to produce an amplification factor of more than a few). These 1D slab models are not realistic enough to confirm our suggested source for the observed diffuse Ly α as being due to resonance scattering in the LHB walls of Ly α photons produced by recombination following photoionization by O and B stars within the LHB, but they strongly point to it as a likely explanation.

These models indicate that the expected line profile of the diffuse Ly α Galactic emissions observed from the solar system would be flat-topped (see internal line profiles, as in R. R. Meier & J. S. Lee 1981) with a full width of ± 0.016 nm, about twice as broad as the backscattered solar line width. Any instruments capable of resolving the Ly α line profile (e.g., Hubble Space Telescope/STIS, MAVEN/IUVS) should expect to see a Galactic background component of roughly $50 \pm 20/0.016 \sim 3125 \pm 1250 \text{ R nm}^{-1}$ over this wavelength interval. More sophisticated 3D radiative transfer calculations are required to make further progress, but it seems plausible that the residual Ly α maps produced here (Figures 7 and 8) may provide

a new way to investigate the interior walls of the LHB. As a start in this direction, in Appendix B we show how the stellar photoionization rate would vary across the LHB wall, and we provide a map of the expected $H\alpha$ brightness due to recombination of neutral H in the LHB walls. This map should be similar to what the $Ly\alpha$ brightness would look like if the emissions were optically thin (instead of the expected value of $\sim 1.3 \times 10^7$ optical depths at line center).

Although our explanation for the observed properties of the residual $Ly\alpha$ map seems plausible, there are several key assumptions that are critical for it to work, some of which are presented in Table 4. We expect that the simplest way to make further progress is to develop a 3D resonance-line radiative transfer code which incorporates the known structure of the LHB, its walls, the local clouds within it, and the hot stars within it.

6. Conclusions

The NH Alice instrument has been used to obtain the first detailed all-sky map of $Ly\alpha$ emission observed from the outer solar system, where the Galactic and solar contributions to the observed brightness are comparable, and the solar contribution can be reasonably removed. The residual $Ly\alpha$ map can then be searched for structures (i.e., sources and sinks) of emissions in the heliosphere and LISM. Near the heliosphere, a brightness enhancement due to a hydrogen wall at the heliopause (e.g., E. Quémerais et al. 2010; V. V. Izmodenov et al. 2013) is not seen, but it is expected to be very large scale and could be present at a ~ 10 R level. No apparent correlations are seen with the boundaries of the four main clouds of the LISM (e.g., S. Redfield & J. L. Linsky 2008); as with the hydrogen wall, these could exist at a ~ 10 R level. Apart from its structure on the 10–20 R level, the overall average brightness level of the $Ly\alpha$ emission of ~ 50 R can be explained as largely due to early-type stars (and hot gas) in the LHB shining on the interior walls of the LHB and photoionizing the HI there. The recombining protons produce $Ly\alpha$ (and concomitant $H\alpha$ and two-photon continuum) emissions, which are resonantly scattered in the walls of the LHB—and across the LHB cavity—until they are approximately isotropic. Since structures like the LHB are fairly common features of galaxies, it may be that the interiors of similar bubbles elsewhere could also be regions of enhanced diffuse $Ly\alpha$ emissions.

A follow-up NH Alice all-sky $Ly\alpha$ map may be made in the future, if possible, and combining that map with this map could result in a considerable improvement in angular resolution. Finally, the maps presented here were obtained using the Alice spectrograph as a photometer, since its spectral resolution is too coarse to resolve the details of the $Ly\alpha$ line structure. However, there are instruments capable of resolving the $Ly\alpha$ line profile (e.g., J. T. Clarke et al. 1998; S. Hosseini & W. M. Harris 2020) which could possibly study this emission in more detail, and thus (even from Earth orbit) provide a new window on the LISM and H populations in the heliosphere.

Acknowledgments

We are grateful to D. Hall for kindly providing the radiative transfer code used to calculate the brightness of backscattered solar $Ly\alpha$ and to A. Goodman for helpful suggestions. We thank the New Horizons team for support: in particular, Gabe Rogers, Debi Rose, and Jon Pineau for planning and executing of the all-sky $Ly\alpha$ observations. This research was supported by NASA New Horizons contract NASW02008 and by SwRI Internal Research Project R6411.

Appendix A Sensitivity of Alice to Diffuse $Ly\alpha$

The all-sky $Ly\alpha$ maps presented here depend on an accurate conversion of the observed Alice total analog count rate into $Ly\alpha$ brightness. In a previous paper (G. R. Gladstone et al. 2021), we found a conversion factor, or sensitivity, of 4.92 ± 0.09 counts $s^{-1} R^{-1}$. However, we now believe that value is too large, because we mistakenly used the *digital* background count rate instead of the *analog* background count rate in deriving the sensitivity. Since the Alice analog count rate is substantially larger than its digital count rate (typically ~ 170 counts s^{-1} compared to ~ 120 counts s^{-1}), the subtracted background was underestimated in G. R. Gladstone et al. (2021), and the derived sensitivity of 4.92 ± 0.09 counts $s^{-1} R^{-1}$ is too large.

This error is corrected here, with the help of several Alice observations made in support of a study of the cosmic optical background (COB), at about the same time period as the all-sky $Ly\alpha$ map, using the LORRI instrument on NH. As reported by M. Postman et al. (2024), 15 observations of the COB were made in a variety of directions (chosen to have as little stellar flux as possible) at high Galactic latitudes. The directions and epochs of the supporting Alice observations are listed in Table 5, along with the measured $Ly\alpha$ brightness in the narrow slit and the total analog Alice count rate. Each Alice observation consisted of eight 1 hr histogram-mode exposures, interleaved with eight 1 hr dark exposures, providing a very deep FUV spectral image in each of the 15 directions.

An example spectral image (with accompanying dark) is shown in Figure 9. The spectral images are truncated in the spectral direction (i.e., the x -direction) to show only the region around the $Ly\alpha$ line, but include all 32 rows of the Alice detector. Each detector row subtends $0^\circ 27'$ on the sky, and the relationship between off-axis angle in the spectral direction and wavelength is $10 \text{ nm degree}^{-1}$, so that the spectral images display the Alice $2^\circ \times 2^\circ + 0.1 \times 4^\circ$ slit in the approximately correct geometric shape.

Since the Alice instrument is calibrated with boresight (row 16) observations of standard stars, we use spectra of that row to determine the integrated $Ly\alpha$ brightness for each of the NCOB observations, e.g., as shown in Figure 10 for NCOB1. Finally, we compare all 15 NCOB observations in Figure 11, the average of which yields a sensitivity of the Alice spectrograph of 3.67 ± 0.02 counts $s^{-1} R^{-1}$.

Table 5
New Horizons NCOB Observations of Specific Sky Directions

Observation ^a	R.A. (deg)	Decl. (deg)	Roll ^b (deg)	l (deg)	b (deg)	B(Ly α) (R)	Analog Rate (counts s ⁻¹)	d_{SUN} (au)	Start Date (UT)	Start MET (s)	End MET (s)
NCOB01	358.4334	-54.9137	90	319.728	-60.293	136.7 \pm 4.7	485.7 \pm 0.9	56.97	2023-09-13 13:56:00	556919276	556981541
NCOB02	5.3540	-55.6590	180	311.662	-60.958	131.5 \pm 4.7	484.3 \pm 0.9	56.86	2023-08-30 18:24:51	555725807	555788037
NCOB03	353.7867	-49.1893	90	331.516	-63.490	133.4 \pm 4.7	490.5 \pm 0.9	56.79	2023-08-21 15:05:51	554936267	554994836
NCOB04	8.0987	-44.4906	135	314.112	-72.222	139.0 \pm 4.7	499.5 \pm 0.9	56.78	2023-08-20 21:46:31	554873907	554932442
NCOB05	10.7611	-27.3461	180	25.794	-88.122	131.9 \pm 4.7	491.7 \pm 0.9	56.84	2023-08-28 14:49:31	555540087	555598622
NCOB06	9.4350	-34.7328	180	323.189	-81.850	136.5 \pm 4.7	489.2 \pm 0.9	56.96	2023-09-12 11:41:40	556824816	556883342
NCOB07	19.0398	-26.6161	180	209.027	-84.464	139.0 \pm 4.8	507.5 \pm 1.0	56.84	2023-08-27 21:42:31	555478467	555537002
NCOB08	336.2651	-30.0473	180	18.925	-57.870	125.2 \pm 4.6	456.8 \pm 0.9	56.86	2023-08-30 01:09:31	555663687	555722222
NCOB09	6.7398	-22.1689	180	73.341	-82.551	133.5 \pm 4.7	489.5 \pm 0.9	56.85	2023-08-29 07:56:31	555601707	555660242
NCOB10	15.7115	-18.8994	180	141.203	-81.364	137.9 \pm 4.8	502.9 \pm 1.0	56.83	2023-08-27 04:36:31	555416907	555475442
NCOB11	10.6266	-15.2837	180	112.541	-77.975	133.9 \pm 4.7	496.5 \pm 1.0	56.83	2023-08-26 06:16:01	555336477	555413182
NCOB12	207.4692	3.9649	0	336.539	62.959	150.6 \pm 4.9	556.5 \pm 1.0	56.75	2023-08-17 04:02:00	554550836	554613057
NCOB13	211.9528	4.6995	0	345.372	61.111	148.2 \pm 4.8	548.9 \pm 1.0	56.75	2023-08-16 10:51:30	554489006	554547532
NCOB14	356.2651	15.5111	135	100.270	-44.420	134.2 \pm 4.7	501.7 \pm 1.0	56.78	2023-08-19 19:27:59	554779195	554837722
NCOB15	247.9273	55.2059	0	84.133	41.702	140.2 \pm 4.8	530.0 \pm 1.0	56.72	2023-08-12 12:56:40	554150916	554209442

Notes.^a As reported in M. Postman et al. (2024).^b Alice slit position angle, measured counterclockwise from the north celestial pole.

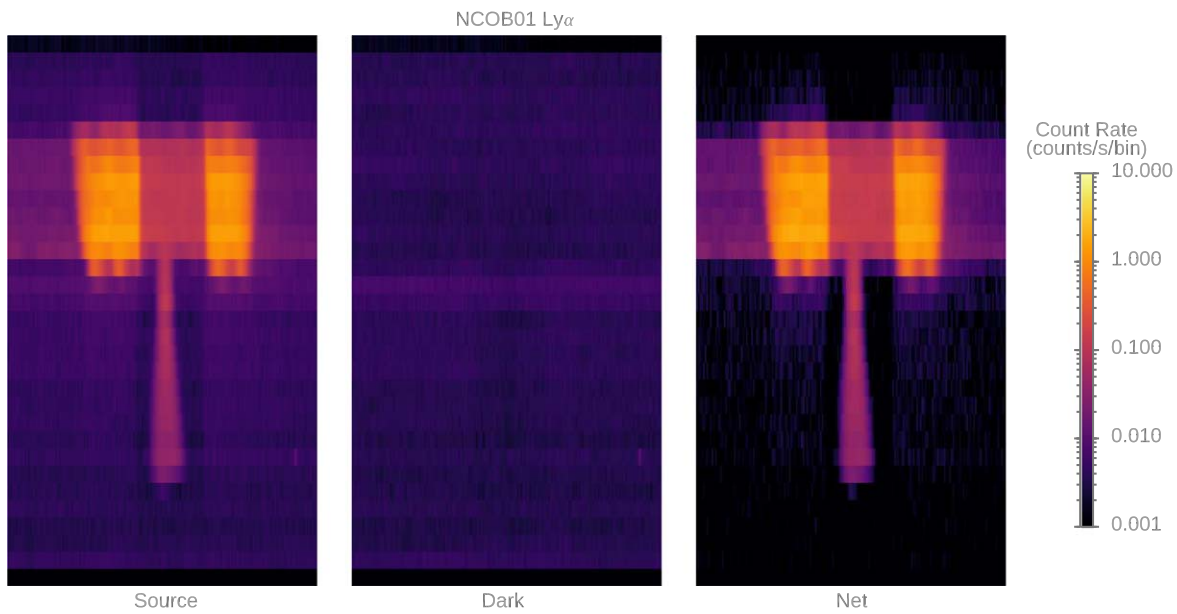


Figure 9. Spectral images for the Alice observation of a dark region on the sky, referred to as NCOB01 (see M. Postman et al. 2024 and Table 5 for more information). Left: the count-rate spectral image of the sum of eight 1 hr histogram exposures of the sky, using all 32 rows and columns 535 through 555 of the Alice detector in order to display the spectral image in the Ly α vicinity. Approximate wavelengths are 120.3–123.9 nm; most of the signal is from diffuse Ly α filling the Alice slit. Center: same as left, but for the sum of the eight 1 hr interleaved dark exposures for observations NCOB01. Right: the net count rate of the sky (left) after subtracting the dark (center) spectral images, showing that the dark sky is completely dominated by diffuse Ly α at FUV wavelengths. The count rate is shown on a log scale in the color bar on the right.

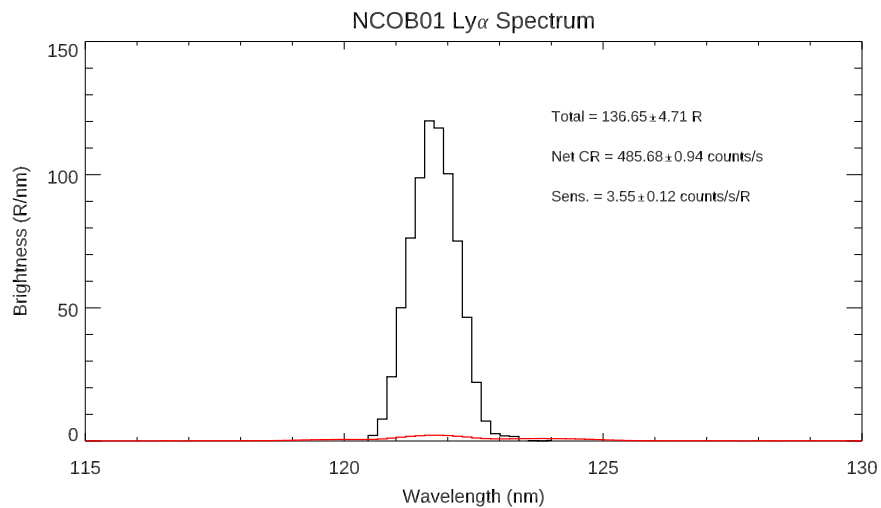


Figure 10. An example spectrum of wavelengths including the diffuse Ly α from the NCOB01 deep exposure, comprised of eight 1 hr exposures interleaved with eight 1 hr darks with the Alice instrument pointed at the direction $(l, b) = (319^\circ 728', -60^\circ 293')$ (see Table 5 for other NCOB information). The observed net brightness spectrum is given by the black histogram, and the 1σ error of the net brightness is shown by the red histogram. As noted on the figure, for this observation the on-axis average diffuse Ly α brightness was 136.65 ± 4.71 R, and the corresponding analog net count rate was 485.68 ± 0.94 counts s^{-1} . These values are combined to give a Ly α sensitivity for the Alice spectrograph of 3.55 ± 0.12 counts s^{-1} R $^{-1}$ for this observation.

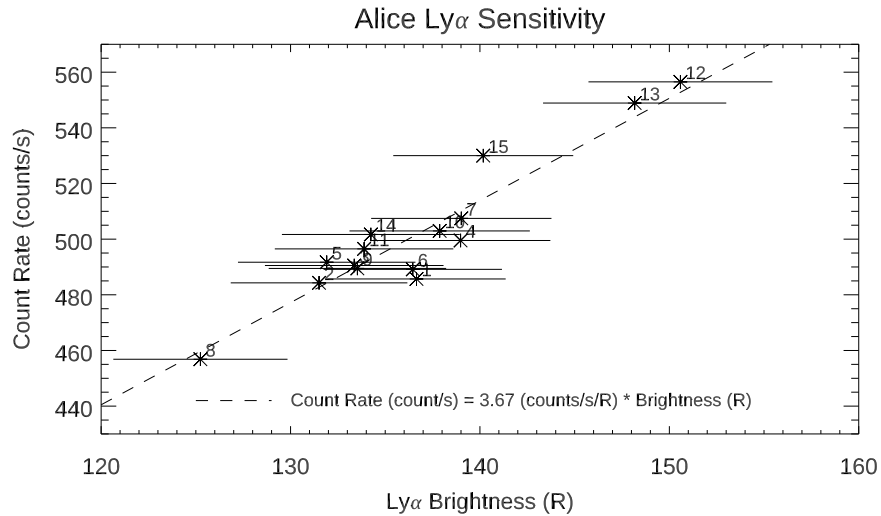


Figure 11. The variation of the Alice spectrograph total analog count rate to observed diffuse Ly α brightness is plotted for the 15 NCOB observations. Using the 15 NCOB measurements, we find an average sensitivity for the Alice spectrograph of $3.67 \pm 0.02 \text{ counts s}^{-1} \text{ R}^{-1}$, which is overplotted as a dashed line. This sensitivity is used to convert the analog count rates observed during the all-sky map into diffuse Ly α brightnesses in regions of the sky uncontaminated by UV-bright stars.

Appendix B

Constraints on H α Produced in the Walls of the Local Bubble

As argued above, the residual all-sky Ly α brightness of $50 \pm 20 \text{ R}$ is likely produced in the walls of the LHB. Sources of Ly α more distant than the outside wall of the LHB would be expected to be less isotropic, i.e., Ly α photons from more distant sources would be more likely to get through the LHB wall if they had already scattered in wavelength into the line wings, and would subtend a smaller solid angle than nearer sources.

Here we estimate the contribution to the observed H α from recombination of hydrogen atoms which have been photoionized by EUV emission from stars within the outer wall of the LHB, in the same process which leads to Ly α emission. This predicted LHB wall H α emission can then be compared with maps of H α (e.g., D. P. Finkbeiner 2003) to search for any correlation. The dust absorption coefficient for H α photons is about one-sixth as large as for Ly α photons (B. T. Draine 2011), so that most of the H α signal comes from sources far beyond the LHB wall, and the contribution from the LHB wall should be no more than a fraction of the total observed signal. We take the LHB to be hot and highly ionized (e.g., S. L. Snowden et al. 2014; J. D. Slavin 2017), so that it is optically thin to EUV photons. At $T = 10^6 \text{ K}$, photochemical equilibrium indicates the HI density expected for a balance between collisional ionization and recombination would be $n_{\text{HI}} \approx 10^{-8} \text{ cm}^{-3}$ or less, since the recombination rate coefficient decreases rapidly at high temperatures. Thus, the EUV photons produced by hot O and B stars in the LHB will first be absorbed when they reach the walls of the LHB. The HI column density in the LHB walls is large ($N_{\text{HI}} > 10^{20} \text{ cm}^{-2}$, with an estimated density $n_{\text{HI}} \approx 3 \text{ cm}^{-3}$; C. Zucker et al.

2022). So we would expect most the EUV flux from the hot LHB stars to photoionize neutral H in the LHB walls. About half of recombinations (actually 0.452, for Case B recombination at $T = 10^4 \text{ K}$ as given by B. T. Draine 2011) following these would lead to an approximately equivalent flux of H α photons.

Using the M. A. Velez et al. (2024) catalog, we find 51 O and B stars in the LHB or the LHB wall (i.e., their distances were less than the distance to the outer LHB wall in the direction of the star, as estimated by T. J. O’Neill et al. 2024). To this list we added three white dwarfs (G191B2B, Feige 24, and HZ43) known to be important sources of EUV radiation near the solar system (e.g., J. Dupuis et al. 1995; B. Y. Welsh et al. 2013). These 54 stars are listed in Table 6, along with their salient properties. We estimated the EUV flux from these stars at each location on the LHB wall, then estimated the H α brightness map that source would produce locally at the LHB wall as seen from Earth, which is shown in Figure 12. Since the recombination yields H α and Ly α are similar, this map effectively shows how the residual all-sky Ly α map shown in Figure 7 would appear if the Ly α photons produced by recombination in the LHB walls were optically thin. As seen in Figure 12, the brightness expected from this source of diffuse H α from the LHB walls is generally only 1 R or less, and it does not contribute much to the total sky brightness of H α (e.g., D. P. Finkbeiner 2003), which is shown on the same brightness scale for comparison. We note that two-photon continuum emissions are also a result of the recombination process (e.g., S. R. Kulkarni 2022); these should be produced at roughly one-half of the production rate of Ly α emissions, and would also be expected to be at the $\sim 1 \text{ R}$ level when integrated over wavelength. Future 3D studies of multiple resonant scattering of Ly α photons in the LHB walls may find this map useful for comparing with their initial Ly α emission rate.

Table 6
Brightest EUV Stars in the Local Hot Bubble

Name ^a	H I Ionization Rate ^b	H I Ionizing Flux ^c	Spectral Type	<i>l</i>	<i>b</i>	Stellar Distance	Outer LHB Wall Distance ^d	$\log N_{\text{HI}}^e$	n_{HI}^e
τ Sco	1.43×10^{-13}	7.52×10^8	B0.2V	351.54	12.81	145.3	164.3	20.5	0.7
μ^2 Sco	7.60×10^{-14}	5.75×10^8	B2IV	346.20	3.86	176.6	205.0
β Cen	6.86×10^{-14}	2.27×10^8	B1III	311.77	1.25	120.2	141.4	19.63	0.12
α Pav	7.91×10^{-14}	5.43×10^7	B2IV	340.90	-35.19	54.8	291.6
α Vir	4.09×10^{-14}	5.39×10^7	B1V	316.11	50.85	76.6	129.4	<19.0	<0.04
γ Cas	7.84×10^{-15}	4.92×10^7	B0.5IVpe	123.58	-2.15	168.4	273.9
γ Ori	2.45×10^{-14}	3.56×10^7	B2V	196.93	-15.95	77.4	170.0
α Ara	2.12×10^{-14}	3.18×10^7	B2Vne	340.76	-8.83	82.0	195.6
σ Sgr	2.21×10^{-14}	2.68×10^7	B2V	9.56	-12.44	69.8	166.3
β Cru	1.57×10^{-14}	2.60×10^7	B1IV	302.46	3.18	85.4	138.1
κ Sco	4.05×10^{-15}	1.97×10^7	B1.5III	351.04	-4.72	148.1	157.6	20.2	0.35
α Mus	9.30×10^{-15}	1.92×10^7	B2IV	301.66	-6.30	96.7	155.1	<20.4	<0.8
FBS 1715+424	3.13×10^{-16}	1.73×10^7	sdOHe0	67.50	34.75	422.2	574.0
κ Cen	2.86×10^{-15}	1.22×10^7	B2IV	326.87	14.75	117.5	191.6	<20.6	<1.1
α^2 Cru	4.43×10^{-15}	9.82×10^6	B1V	300.13	-0.36	99.0	207.6
ζ CMa	2.48×10^{-15}	9.15×10^6	B2.5V	237.52	-19.43	111.1	284.9
BD+25 4655	2.29×10^{-15}	8.96×10^6	sdO6	81.67	-22.36	115.5	230.1
α^1 Cru	3.85×10^{-15}	8.62×10^6	B0.5IV	300.13	-0.36	99.0	207.6
BD+28 4211	2.21×10^{-15}	8.62×10^6	sdO2V8He5	81.87	-19.29	112.1	215.3
β Lup	2.61×10^{-15}	7.38×10^6	B2III	326.25	13.91	117.4	191.3	20.4	0.7
η Cen	3.46×10^{-15}	6.72×10^6	B2Ve	322.77	16.67	93.7	192.9
β Mus	2.70×10^{-15}	6.54×10^6	B2V+B3V	302.45	-5.24	104.7	155.5
γ Lup	1.35×10^{-15}	4.60×10^6	B2IV	333.19	11.89	129.0	189.9	<20.3	<0.5
η Lup	1.18×10^{-15}	4.21×10^6	B2.5IV	338.77	11.01	131.7	185.1
BD+48 1777	3.43×10^{-16}	3.89×10^6	sdO9:	170.34	46.04	236.1	335.5
c Ori	7.22×10^{-16}	3.76×10^6	B1V	208.50	-19.11	153.5	174.5
HD 64740	2.94×10^{-16}	3.61×10^6	B2V	263.38	-11.19	244.8	277.7
θ Oph	9.84×10^{-16}	3.59×10^6	B2IV	0.46	6.55	133.7	166.8	<20.5	<0.8
η UMa	1.29×10^{-14}	3.38×10^6	B3V	100.70	65.32	31.9	361.6	<21.0	<1.0
ζ Cen	9.85×10^{-16}	2.80×10^6	B2.5IV	314.07	14.19	117.7	189.9
β Cep	3.05×10^{-16}	2.76×10^6	B0.5III	107.54	14.03	210.1	291.4	19.93	0.13
κ CMa	3.13×10^{-16}	2.76×10^6	B1.5Ve	242.36	-14.49	207.0	270.7
ϕ Cen	6.83×10^{-16}	2.76×10^6	B2IV	315.98	19.07	140.8	189.7
α Lup	6.19×10^{-16}	2.51×10^6	B1.5III	321.61	11.44	142.5	209.6	<19.3	<0.04
δ Cet	3.10×10^{-16}	2.42×10^6	B2IV	170.76	-52.21	194.9	258.0
δ Lup	5.14×10^{-16}	2.32×10^6	B1.5IV	331.32	13.82	148.6	189.0	<20.2	<0.4
BD+39 3226	2.92×10^{-16}	2.13×10^6	sdOHe	65.00	28.77	189.2	281.3
β Sco	6.35×10^{-16}	2.02×10^6	B1V+B2V	353.19	23.60	120.0	121.1	21.0	2.7
ϵ Car	2.75×10^{-16}	1.93×10^6	B2:V+K3:III	274.29	-12.60	185.5	270.1
ϵ Lup	2.84×10^{-16}	1.91×10^6	B2IV-V	329.23	10.32	157.0	191.3
ζ Tau	5.04×10^{-16}	1.91×10^6	B1IVe_shell	185.69	-5.64	136.4	174.0
δ Cen	2.98×10^{-16}	1.87×10^6	B2Vne	296.00	11.57	174.9	209.6
δ Cru	4.58×10^{-16}	1.82×10^6	B2IV	298.23	3.79	139.5	207.9	<20.2	<0.4
ν Cen	5.56×10^{-16}	1.75×10^6	B2IV	314.41	19.89	124.3	190.1
β CMa	3.49×10^{-16}	1.62×10^6	B1II-III	226.06	-14.27	151.1	191.7	18.26	0.0039
θ Car	3.91×10^{-16}	1.57×10^6	B0Vp	289.60	-4.90	139.7	205.4	20.26	0.42
γ Peg	3.55×10^{-16}	1.50×10^6	B2IV	109.43	-46.68	143.9	264.7	<20.2	<0.4
ϵ CMa	4.73×10^{-16}	1.49×10^6	B1.5II	239.83	-11.33	124.2	291.9	17.78	0.0016
BD+75 325	3.44×10^{-16}	1.49×10^6	sdO5	139.51	31.25	145.4	277.0
ϵ Cen	4.03×10^{-16}	1.41×10^6	B1III	310.19	8.72	131.1	205.8	<19.9	<0.2
ζ Cas	2.87×10^{-16}	1.32×10^6	B2IV	120.78	-8.91	150.0	170.1
Feige 24	5.98×10^{-16}	1.15×10^6	DA1+dM C	165.97	-50.27	77.7	191.3	18.45	0.012
G191B2B	1.12×10^{-15}	9.73×10^5	DA.8 C	155.95	7.10	52.5	143.90	18.18	0.0094
HZ43	2.23×10^{-16}	2.49×10^5	DAwk D	54.11	84.16	60.3	453.5	17.93	0.0046
Total:	5.69×10^{-13}								

Notes.

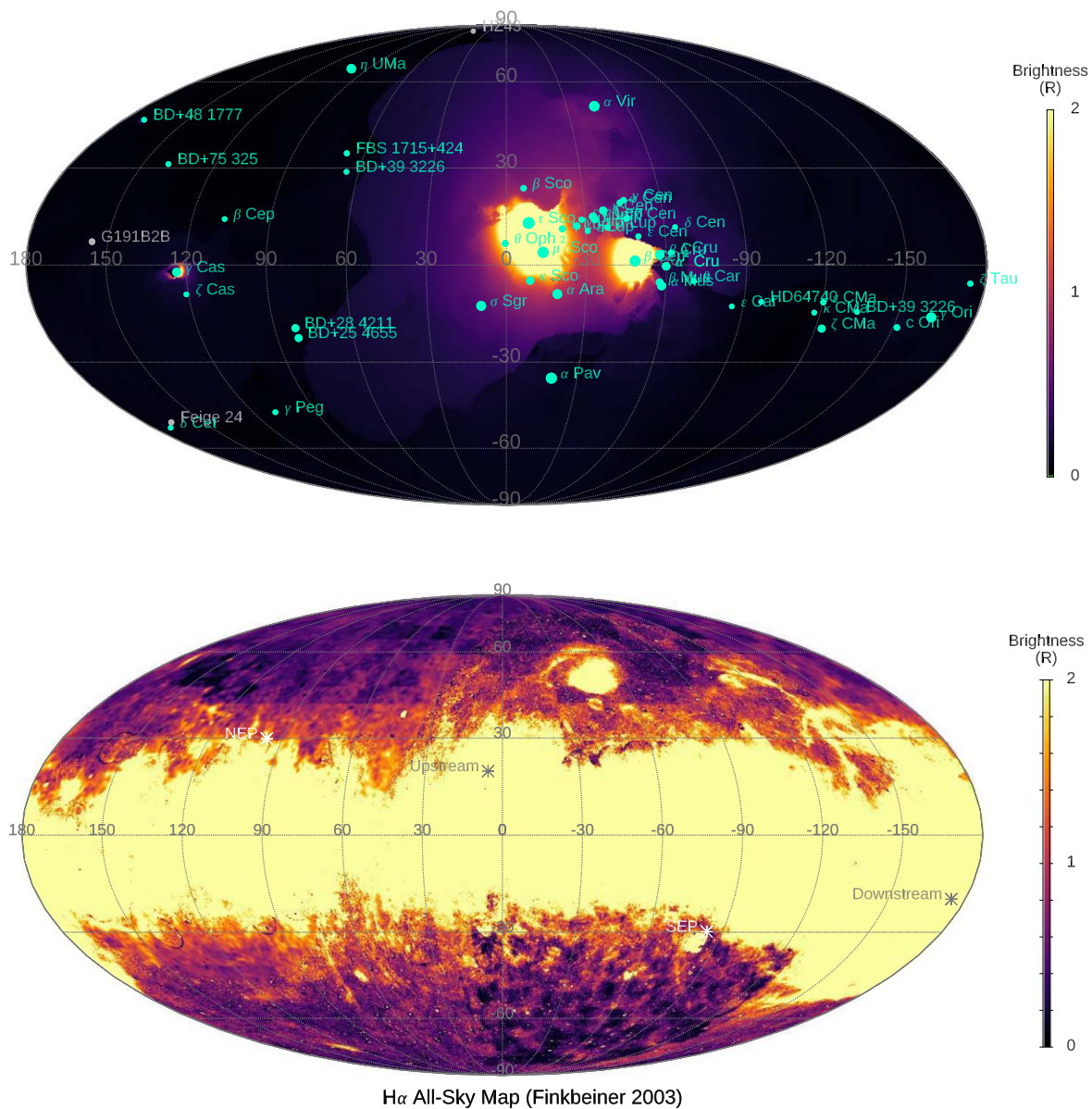
^a Unless otherwise noted, the stellar properties listed here are taken from SIMBAD (<https://simbad.u-strasbg.fr/simbad/sim-fid>).

^b Estimated H I photoionization rate outside the LIC. Note that the EUV spectra of these stars are based on model fits to their FUV spectra and are likely underestimates (see, for ϵ CMa, the estimated EUV flux derived by J. M. Shull et al. 2025 is $\sim 30\times$ larger than given here).

^c Estimated H I photoionization flux at 1 pc from the star; the table is ordered by this value. Note that the EUV spectra of these stars are based on model fits to their FUV spectra and are likely underestimates.

^d Distance to the outer wall of the LHB in the star direction, as determined by T. J. O'Neill et al. (2024).

^e Interstellar H I column density (where available) from A. Diplas & B. D. Savage (1994), J. M. Shull et al. (2025), J. T. Cassinelli et al. (1996), M. Lemoine et al. (2002), J. W. Kruk et al. (2002), and J. Dupuis et al. (1995), and H I average number density from dividing the column density by the distance to the star.



H α All-Sky Map (Finkbeiner 2003)

Figure 12. The upper panel shows the estimated brightness of H α emissions from the wall of the LHB that would result from EUV illumination by hot stars within the LHB, followed by local recombination and emission. The location of the outer edge of the LHB, as provided in T. J. O’Neill et al. (2024), was used in this calculation, along with the radiation field estimated using the stars in Table 6, which are labeled with dots sized according to their estimated H I photoionizing flux at a distance of 1 pc. The brightest regions are near the primary O-B associations mentioned above at the end of Section 4. The lower panel shows a high-resolution map of diffuse H α emissions (D. P. Finkbeiner 2003); the lack of correlation with the model map of expected H α from the interior wall of the LHB is likely due to the domination of contributions from beyond the outer wall of the LHB.

ORCID iDs

G. Randall Gladstone <https://orcid.org/0000-0003-0060-072X>
 J. Michael Shull <https://orcid.org/0000-0002-4594-9936>
 Wayne R. Pryor <https://orcid.org/0000-0001-8112-8783>
 Jonathan Slavin <https://orcid.org/0000-0002-7597-6935>
 Joshua A. Kammer <https://orcid.org/0000-0002-3441-3757>
 Tracy M. Becker <https://orcid.org/0000-0002-1559-5954>
 Tod R. Lauer <https://orcid.org/0000-0003-3234-7247>
 Marc Postman <https://orcid.org/0000-0002-9365-7989>
 John R. Spencer <https://orcid.org/0000-0003-4452-8109>
 Joel Wm. Parker <https://orcid.org/0000-0002-3672-0603>
 Kurt D. Retherford <https://orcid.org/0000-0001-9470-150X>
 Michael A. Velez <https://orcid.org/0000-0001-5835-2250>

Maarten H. Versteeg <https://orcid.org/0000-0002-2503-9492>
 Michael W. Davis <https://orcid.org/0000-0003-4338-1635>
 Cynthia S. Froning <https://orcid.org/0000-0001-8499-2892>
 Camden D. Ertley <https://orcid.org/0000-0003-0187-6699>
 Nathaniel Cunningham <https://orcid.org/0000-0002-8957-7310>
 Jayant Murthy <https://orcid.org/0000-0003-4034-5137>
 Richard C. Henry <https://orcid.org/0000-0003-4447-2686>
 Seth Redfield <https://orcid.org/0000-0003-3786-3486>
 Carey M. Lisse <https://orcid.org/0000-0002-9548-1526>
 Kelsi N. Singer <https://orcid.org/0000-0003-3045-8445>
 Anne J. Verbiscer <https://orcid.org/0000-0002-3323-9304>
 Pontus C. Brandt <https://orcid.org/0000-0002-4644-0306>
 S. Alan Stern <https://orcid.org/0000-0001-5018-7537>

References

- Adams, T. F. 1971, *A&A*, **12**, 280
- Baranov, V. B., Lebedev, M. G., & Malama, Y. G. 1991, *ApJ*, **375**, 347
- Baranov, V. B., & Malama, G. 1993, *JGR*, **98**, 15157
- Bertaux, J.-L., & Blamont, J. E. 1971, *A&A*, **11**, 200
- Cassinelli, J. T., Cohen, D. H., MacFarlane, J. J., et al. 1996, *ApJ*, **460**, 949
- Clarke, J. T., Lallement, R., Bertaux, J.L., et al. 1998, *ApJ*, **499**, 482
- Costa, J., Lallement, R., Quémerais, E., et al. 1999, *A&A*, **349**, 660
- Cox, D. P., & Reynolds, R. J. 1987, *ARA&A*, **25**, 303
- Dijkstra, M. 2014, *PASA*, **31**, e040
- Dijkstra, M. 2019, in *Lyman-alpha as an Astrophysical and Cosmological Tool*, ed. A. Verhamme et al. Vol. 46 (Berlin: Springer), 1
- Diplas, A., & Savage, B. D. 1994, *ApJS*, **93**, 211
- Draine, B. T. 2011, *Physics of the Interstellar and Intergalactic Medium* (Princeton, NJ: Princeton Univ. Press)
- Dupuis, J., Vennes, S., Bowyer, S., et al. 1995, *ApJ*, **455**, 574
- Fahr, H. J. 1974, *SSRv*, **15**, 483
- Finkbeiner, D. P. 2003, *ApJS*, **146**, 407
- Frisch, P. C., Redfield, S., & Slavin, J. D. 2011, *ARA&A*, **49**, 237
- Gladstone, G. R. 1982, *JQSRT*, **27**, 545
- Gladstone, G. R., Stern, S. A., & Pryor, W. R. 2013, in *Cross-Calibration of Far UV Spectra of Solar System Objects and the Heliosphere*, ed. E. Quémerais, M. Snow, & R. M. Bonnet, Vol. 13 (New York: Springer), 177
- Gladstone, G. R., Pryor, W. R., Hall, D. T., et al. 2021, *AJ*, **162**, 241
- Gladstone, G. R., Pryor, W. R., & Stern, S. A. 2015, *Icar*, **246**, 279
- Gladstone, G. R., Pryor, W. R., Stern, S. A., et al. 2018, *GeoRL*, **45**, 8022
- Gry, C., & Jenkins, E. B. 2014, *A&A*, **567**, A58
- Hall, D. T. 1992, PhD thesis, Univ. Arizona
- Hall, D. T., Shemansky, D. E., Judge, D. L., et al. 1993, *JGR*, **98**, 15185
- Hosseini, S., & Harris, W. M. 2020, *JATIS*, **6**, 015005
- Izmodenov, V. V., Katushkina, O. A., Quémerais, E., & Bzowski, M. 2013, in *Cross-Calibration of Far UV Spectra of Solar System Objects and the Heliosphere*, ed. E. Quémerais, M. Snow, & R. M. Bonnet, Vol. 13 (New York: Springer), 7
- Katushkina, O. A., Quémerais, E., Izmodenov, V. V., et al. 2016, *JGR*, **121**, 93
- Katushkina, O. A., Quémerais, E., Izmodenov, V. V., et al. 2017, *JGR*, **122**, 10,921
- Kulkarni, S. R. 2022, *PASP*, **134**, 084302
- Kruk, J. W., Howk, J. C., André, M., et al. 2002, *ApJS*, **140**, 19
- Lallement, R. E., Vidal-Madjar, A., & Ferlet, R. 1986, *A&A*, **168**, 225
- Lemaire, P., Charra, J., Jouchoux, A., et al. 1978, *ApJ*, **223**, L55
- Lemoine, M., Vidal-Madjar, A., Hébrard, G., et al. 2002, *ApJS*, **140**, 67
- Linsky, J. L., & Redfield, S. 2021, *ApJ*, **920**, 75
- Meier, R. R. 1977, *A&A*, **55**, 211
- Meier, R. R. 1991, *SSRv*, **58**, 1
- Meier, R. R., & Lee, J. S. 1981, *ApJ*, **250**, 376
- Münch, G. 1962, in *Space Age Astronomy*, ed. A. J. Deutsch & W. B. Klemperer (New York: Academic), 219
- O'Neill, T. J., Zucker, C., Goodman, A. A., & Edenhofer, G. 2024, *ApJ*, **973**, 136
- Østgaard, N., Mende, S. B., Frey, H. U., et al. 2003, *JGRA*, **108**, 1300
- Postman, M., Lauer, T. R., Parker, J. W., et al. 2024, *ApJ*, **972**, 95
- Pryor, W. R., Holsclaw, G. M., McClintock, W. E., et al. 2013, in *Cross-Calibration of Far UV Spectra of Solar System Objects and the Heliosphere*, ed. E. Quémerais, M. Snow, & R. M. Bonnet, Vol. 13 (New York: Springer), 163
- Quémerais, E., Lallement, R., Bertaux, J.-L., et al. 2010, *ApJ*, **711**, 1257
- Quémerais, E., Sandel, B. R., Izmodenov, V. V., & Gladstone, G. R. 2013, in *Cross-Calibration of Far UV Spectra of Solar System Objects and the Heliosphere*, ed. E. Quémerais, M. Snow, & R. M. Bonnet, Vol. 13 (New York: Springer), 141
- Redfield, S., & Linsky, J. L. 2008, *ApJ*, **673**, 283
- Shull, J. M., Curran, R. M., & Topping, M. W. 2025, *ApJ*, **979**, 21
- Shull, J. M., & Kulkarni, S. R. 2023, *ApJ*, **951**, 35
- Slavin, J. D. 2017, *PhCS*, **837**, 012011
- Snowden, S. L., Chiao, M., Collier, M. R., et al. 2014, *ApJL*, **791**, L14
- Stern, S. A., Slater, D. C., Scherrer, J., et al. 2008, *SSRv*, **140**, 155
- Swaczyna, P., McComas, D. J., Zirnstein, E. J., et al. 2020, *ApJ*, **903**, 48
- Thomas, G. E. 1978, *AREPS*, **6**, 173
- Thomas, G. E., & Blamont, J. E. 1976, *A&A*, **51**, 283
- Vallerga, J. V., & McPhate, J. B. 2000, *Proc. SPIE*, **4139**, 34
- Velez, M. A., Retherford, K. D., Hue, V., et al. 2024, *PSJ*, **5**, 93
- Welsh, B. Y., Vedder, P. W., Vallerga, J. V., & Craig, N. 1991, *ApJ*, **381**, 462
- Welsh, B. Y., Wheatley, J., Dickinson, N. J., & Barstow, M. A. 2013, *PASP*, **125**, 644
- Woods, T., Tobiska, W. K., Rottman, G. J., & Worden, J. R. 2000, *JGR*, **105**, 27,195
- Zucker, C., Goodman, A. A., Alves, J., et al. 2022, *Natur*, **601**, 334